ACS APPLIED MATERIALS & INTERFACES

Research Article

www.acsami.org

Graphene-Based Bioinspired Compound Eyes for Programmable Focusing and Remote Actuation

Lanlan Wang,[#] Fang Li,[#] Hongzhong Liu,[*] Weitao Jiang,[*] Dong Niu, Rui Li, Lei Yin, Yongsheng Shi, and Bangdao Chen

State Key Laboratory for Manufacturing Systems Engineering, Xi'an Jiaotong University, Xi'an 75049, China

Supporting Information

ABSTRACT: Inspired by creatures' eyes, bioinspired compound eyes (BCEs) endowed with larger fields of view and vari-focal capability are extremely appealing in micro-optical devices. However, the present actuation strategies of BCEs commonly demand complicated fields, e.g., electro-wetting actuation, dielectrophoretic drive and pressure gradient, which greatly limits their practical applications. In this work, the photothermal conversion of graphene nanosheets (GNSs) is first utilized to fabricate lenslets toward BCEs. Under the actuation of near-infrared (nIR) pulsed laser, GNSs absorb photo energy and convert it to thermal energy, which increases the temperature of lenslets and then leads to the adjustment of lenslet curvature. At a result, BCEs manifest a reversible 4-fold zoom and a wide FOV up to 160°. In addition, BCEs also perform the programmable focusing by selectively confining nIR laser to a vari-focal region. In contrast with traditional BCEs, graphene-based BCEs are versatile with wide FOV and vari-focal ability by nIR actuation. Herein, these excellent properties make graphene-based BCEs promising for remote-driven microfluidic devices.

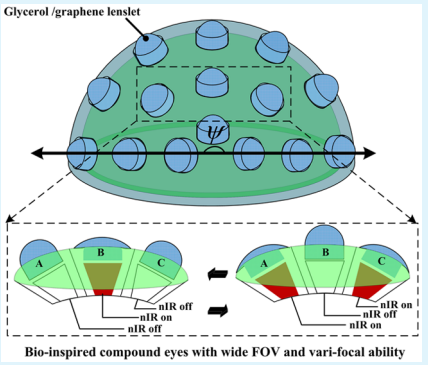

Bio-inspired compound eyes with wide FOV and vari-focal ability

KEYWORDS: *bioinspired compound eyes (BCEs), graphene nanosheets (GNSs), photothermal energy conversion, tunable focusing, remote actuation*

1. INTRODUCTION

Microlens array has been currently used as a highly parallel image projection to enable unique focusing and collimation abilities.[1] Particularly, bioinspired compound eyes (BCEs) constituted by microlens array have diverse applications, e.g., various imaging sensors, three-dimensional (3D) displays, and photodetectors.[2−4] Although microlens array technology has been greatly advanced as a result of novel fabrication methods and optical quality, the current BCEs typically have fixed focal lengths and relatively large diameters.[2,5,6] In nature, insects' compound eyes offer a panoramic field of view (FOV) up to 240°.[7,8] When an object moves across the visual field of drosophila compound eye, each ommatidium is responsible for one area in space, that is, programmable focusing.[9] Otherwise, the eyes of vertebrates can focus on different distances through adjusting lens shape under the assistance of ciliary muscles.[10] Inspired by these eyes, it is extremely attractive to fabricate BCEs with advantages of both insects' compound eyes and vertebrates' single-lens eyes, that is, large FOV and programmable vari-focal capability (Figure 1). In the past decade, large FOV was normally realized by maximizing the density of lenslets on a hemispheric dome.[11,12] For the vari-focal ability of BCEs, an external force, e.g., electro-wetting actuation, dielectrophoretic drive, and pressure gradient, was commonly employed.[13−15] However, electrowetting and dielectrophoretic actuation require a complicated electrical circuit to supply relatively high voltage (up to 200 V), which causes inevitable hysteresis, electric breakdown, and analyte redox reactions to substantially decrease device stability. Similarly, pressure gradient cannot avoid deformable actuators, making their integration in space a challenge. Thereby, it is extremely necessary to develop novel actuating approaches toward BCEs.

In recent years, the dispersion of photothermal material into microfluidics opens up a new interdisciplinary technology of optofluidics.[16,17] Specifically, due to its superior photothermal conversion, graphene, a two-dimensional atom-thick carbon nanosheet, has drawn considerable attention in biomedical imaging, phototherapy, photoelectric fields, and noninvasive manipulation of fluids.[18−20] Under illumination of near-infrared (nIR) light, the photothermal conversion of graphene nanosheets (GNSs) involves the absorption of incident photons and thermal release, eventually resulting in elevated temperature of surrounding liquid.[21] Therefore, graphene is a promising material to realize the vari-focal capability of BCEs without sacrificing the density of liquid lenslets.

In this work, we have utilized GNSs for light-actuated BCEs with large FOV and programmable focusing capability, as demonstrated in Figure 1a. Through a template-directed self-assembly process, glycerol/graphene nanosheets (G/GNSs) based BCEs were constructed. As shown in Figure 1b, G/GNSs lenslets are uniformly arranged on a hemispherical dome, which provides a large FOV up to 160°. Under remote nIR laser light irradiation, GNSs endow BCEs with reversible 4-fold and

Received: July 15, 2015
Accepted: September 11, 2015
Published: September 11, 2015

DOI: 10.1021/acsami.5b06361
ACS Appl. Mater. Interfaces 2015, 7, 21416−21422

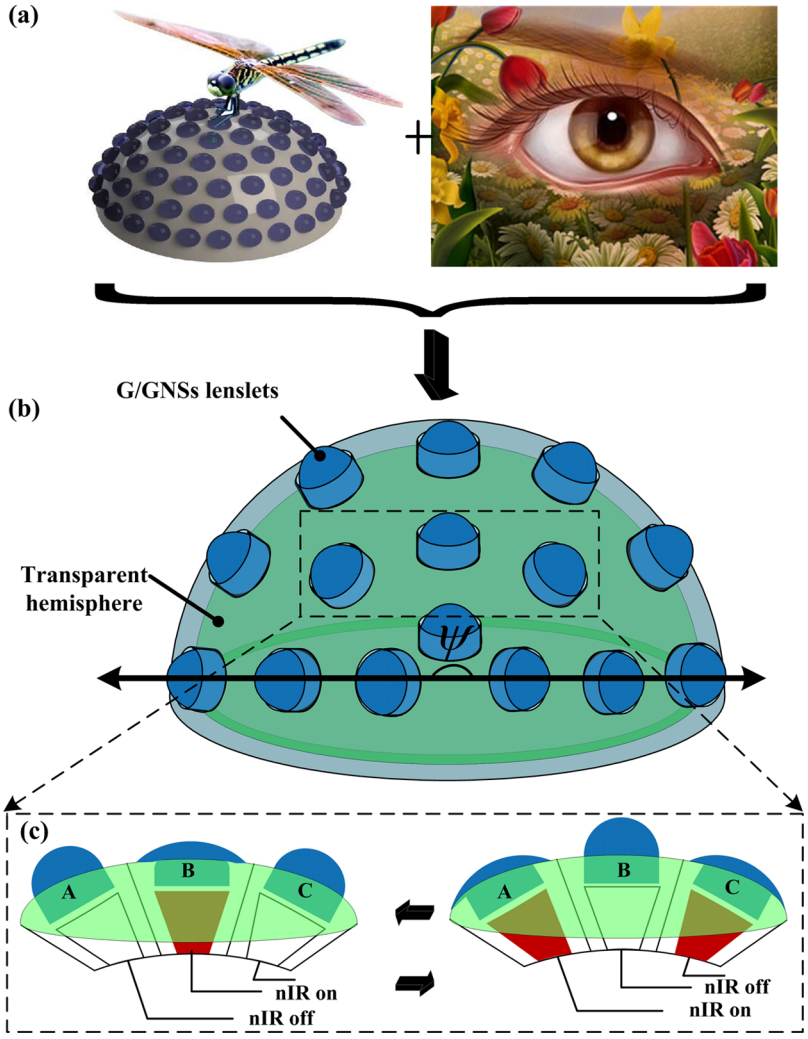

Figure 1. BCEs with wide FOV and vari-focal ability: (a) Insects' compound eyes and vertebrates' single-lens eye offer panoramic FOV and varifocal ability, respectively. (b) High-density lenslets are omnidirectionally distributed on a hemispheric dome to realize panoramic FOV (ψ). (c) GNSs functioning as ciliary muscle endow BCEs with programmable vari-focusing and remote actuating under nIR irradiation.

programmable varifocal ability (Figure 1c); that is, each lenslet can be tunable on demand like human eyes. Herein, graphene-based BCEs show potential utilization in adaptive optical systems such as three-dimensional imager,[22] point-of-care diagnostic,[23] and real-time motion tracking[24] without any physical valves or mechanical pumping devices.

2. EXPERIMENTAL SECTION

Synthesis of GNSs. Glycerol containing GNSs was explored as functional G/GNSs solution (Figure S1). A desired amount of GNSs (4 mg) was well dispersed into glycerol (100 mL) by ultrasonication. GNSs were synthesized from natural graphite flakes by a modified Hummers method.[25] The TEM image and corresponding selected area electron diffraction (SAED) pattern indicate sheet-like morphology (Figure S1a). In order to further investigate the transparency of as-prepared BCEs, the transmittance spectrum was tested (Figure S1d). The transparency of GNSs is determined to be ~98% at the wavelength from 400 to 1000 nm.

Microfabrication of BCEs. A transparent hemispheric dome with uniform microcavity array (MCA) was constructed by a reconfigurable microtemplating process (Figure S2) and then served as the template. In order to uniformly assemble G/GNSs droplets into MCA template, a beaker with glycerol was placed in an assembly system (Figure S2e). The moving velocity of the template was kept at 0.32 mm/s by a stepper motor and temperature was accurately guided to be 15 °C via a Peltier element. When the template was dragged out from solution, the droplet at the micromeniscus−substrate interface was adsorbed into the microcavity by the breakup of capillary. Finally, uniform BCEs were achieved (Figure S2f).

nIR Actuation of BCEs. To achieve programmable focusing and remote actuation, a nIR light source with a wavelength of 808 nm and power density of 2.0 W/cm^2 was utilized. The light density was recorded with THORLAB PM200D intensity meter. The angular acceptance was directly measured by three-dimensional optical sectioning with a modified transmissive confocal microscope. The incident light was first collected by lenslets, then magnified by an objective lens and finally detected with a charge-coupled device (CCD). When light was incident from a certain angle, the objective lens was well rotated to receive the light signal. The repeatability of BCEs was investigated by multicycle actuation over 1 week.

3. RESULTS AND DISCUSSION

3.1. Fabrication and Characterizations of BCEs.

Graphene-based BCEs with a large FOV are prepared using a simple template-directed self-assembly method. Scanning electrical microscopy (SEM) image in Figure 2a reveals that MCA template was composed of ~900 microcavities, in which each diameter was 100 μm. Second, a template-directed self-assembly system was managed in Figure 2b. When the template

DOI: 10.1021/acsami.5b06361
ACS Appl. Mater. Interfaces 2015, 7, 21416−21422

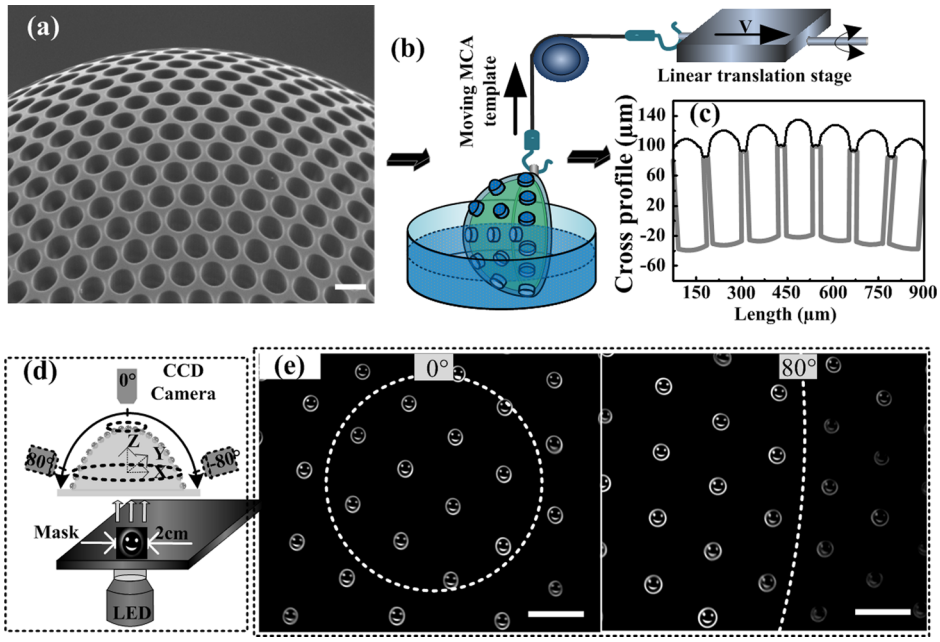

Figure 2. Fabrication process of BCEs: (a) SEM image of a transparent hemisphere dome with microcavity array (MCA). (b) Lenslets arranged on the hemispherical dome via MCA-directed assembly process. (c) Cross profile of BCEs are measured by a LSCM. (d) Sketch of angular acceptance by a modified transmissive confocal microscope; (e) Captured images by two CCD cameras at two distinct angles of 0° (center) and 80°, respectively. Scale bar is 100 μm.

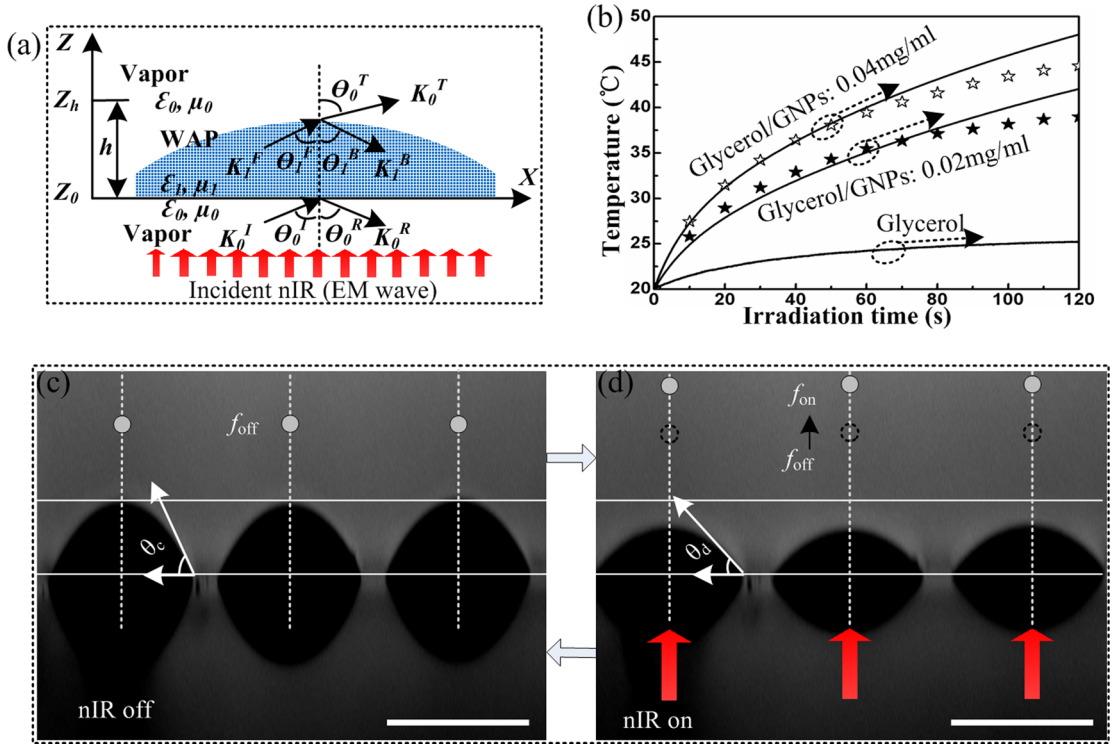

Figure 3. Photothermal-to-hydrodynamic energy conversion mechanism. (a) Model of G/GNSs lenslets subjects to a nIR incident light (EM plane wave). (b) Lenslet temperature-dependence of irradiation time: obviously improved temperature was noted for the lenslet with a concentration of 0.04 mg/mL, in contrast with 0.02 mg/mL and glycerol without GNSs. The optical photographs show G/GNSs lenslets (at a concentration of 0.04 mg/mL) convergent with light-off (c) and divergent with light-on (d).

was dragged out from solution, the droplet formed at the micromeniscus−substrate interface filled in the microcavity. Finally, liquid lenslets were obtained and each droplet in a microcavity has a circular diameter of 100 μm and a period of 115 μm (Figure 2c). The height of the lenslet was determined to be ~30 μm by features of moving contact line (Figure 2c), which was first appreciated by Huh and Scriven (1971).[26] They revealed that there was a viscosity-induced pressure on the free surface. This pressure must be balanced by capillary pressure and hence requires a curvature of interface.[27]

DOI: 10.1021/acsami.5b06361
ACS Appl. Mater. Interfaces 2015, 7, 21416−21422

In order to demonstrate the FOV of fabricated BCEs, the imaging experiment was conducted, as shown in Figure 2d. When light is incident onto the BCEs, every lenslet produces a focal image - "smiley face". Thus, as the CCD camera shifts from 0° (center) to 80°, the "smiley face" pattern appears on the detector surface. These "smiley face" patterns possess high optical uniformity along the $X-Y$ plane in Figure 2e. Therefore, the focused images of "smiley face" have a strong optical contrast with the background, without noticeable off-axis aberration, distortion, or blur. It indicates the capability of real-time motion-tracking and wide FOV up to 160°.

3.2. Mechanism of Graphene-Based Photothermal Conversion. The photothermal energy conversion of GNSs and tunable focusing capability of liquid lens can be explained by Maxwell's electromagnetic wave theory, which is assumed to be a homogeneous wave-absorbing plate as shown in Figure 3a, and then, the thermodynamic method is introduced to describe the mechanism of photothermal energy conversion.[28,29] Based on Maxwell's equations, the distributions of electric field and magnetic field in G/GNSs lenslet (E_y and H_x) and in vapor (E_{y0} and H_{x0}) can be, respectively, expressed as eqs 1 and 2:[30,31]

$$\left.\begin{aligned} E_y(z,t) &= (A\mathrm{e}^{-\gamma_1 z\cos\theta^F} + B\mathrm{e}^{\gamma_1 z\cos\theta^B})\mathrm{e}^{\gamma_0\sin\theta_0 x}\mathrm{e}^{j\omega t} \\ -H_x(z,t) &= \frac{\gamma_1}{j\omega\mu_1}(\cos\theta^F A\mathrm{e}^{-\gamma_1 z\cos\theta^F} \\ &\quad - \cos\theta^B B\mathrm{e}^{\gamma_1 z\cos\theta^B})\mathrm{e}^{\gamma_0\sin\theta_0 x}\mathrm{e}^{j\omega t} \end{aligned}\right\} \quad (1)$$

$$\left.\begin{aligned} E_{y0} &= (A_0\mathrm{e}^{-\gamma_0 z\cos\theta_0^I} + B_0\mathrm{e}^{\gamma_0 z\cos\theta_0^R})\mathrm{e}^{\gamma_0\sin\theta_0 x}\mathrm{e}^{j\omega t} \\ -H_{x0} &= \frac{\gamma_0}{j\omega\mu_0}(\cos\theta_0^I A_0\mathrm{e}^{-\gamma_0 z\cos\theta_0^I} \\ &\quad - \cos\theta_0^R B_0\mathrm{e}^{\gamma_0 z\cos\theta_0^R})\mathrm{e}^{\gamma_0\sin\theta_0 x}\mathrm{e}^{j\omega t} \end{aligned}\right\} \quad (2)$$

where superscripts I, R, F, and B denote the incident, reflected, forward, and backward waves, respectively. ω and θ_0 are the angular frequency and incident angle of the electromagnetic wave, respectively. A, B, A_0, and B_0 denote amplitude factor. Reflection coefficient is defined as $R = (z - z_0)/(z + z_0)$, in which $Z = Z_0(\mu_r/\in_r)^{1/2}$ is impedance and the impedance in free space is $Z_0 = (\mu_0/\in_0)^{1/2}$.

Here, $\gamma_i = [(j\omega\varepsilon_i)\ (j\omega\mu_i)]^{1/2}$ $(i = 0, 1)$, $\theta^F = \theta^B = \theta = \cos^{-1}[1 - (\gamma_0 \sin\theta_0/\gamma_1)^2]^{1/2}$, $\theta_0^I = \theta_0^R = \theta_0$, $\varepsilon_1 = \varepsilon_1' - j\varepsilon_1''$, and $\mu_1 = \mu_1' - j\mu_1''$ are complex permittivity and complex permeability in G/GNSs lenslet; ε_0 and μ_0 are permittivity and permeability of vapor.

Generally, absorbing materials always dissipate incident electromagnetic wave energy by converting it into heat. Based on the Poynting vector theorem, the absorbed energy in G/GNSs lenslet can be given as

$$Q(z,t) = \frac{\omega}{2}\varepsilon_0\varepsilon_1''|E_y(z,t)|^2 + \frac{\omega}{2}\mu_0\mu_1''|H_x(z,t)|^2 \quad (3)$$

Then energy balance in the solution can be described as

$$\rho c_v\frac{\partial T}{\partial t} = \frac{\partial}{\partial z}\left[\lambda\frac{\partial T}{\partial z}\right] + Q(z,t) \quad (4)$$

In the above equations, material properties, such as density ρ, specific heat C_v and thermal conductivity λ, are the effective values of solution. These parameters can be obtained by volume averaging method $\overline{f_{eff}} = V_1 f_1 + V_2 f_2$, in which V_1 and V_2 are volume fraction of GNSs and glycerol, and f_1 and f_2 denote their fraction. In this paper, the material parameters of GNSs and glycerol are $\rho_1 = 20g/L$, $\rho_2 = 1.263g/cm^3$, $c_{v1} = 710\ \mathrm{J/(kg{\cdot}K)}$, $c_{v2} = 2.4 \times 10^3\ \mathrm{J/(kg{\cdot}K)}$, $\lambda_1 = 5300\ \mathrm{W/mK}$, $\lambda_2 = 0.285\ \mathrm{W/mK}$, which are assumed independently on temperature T. However, the complex permittivity of G/GNSs lenslet behaves dependence on wave absorption, which is highly affected by temperature variation. So, in our model, the dielectric parameters ε' and ε'' are both dependent on temperature and assumed to be an exponential function[32] based on nIR absorption characteristics of GNSs. Furthermore, considering that glycerol is nonmagnetic and the permeability of GNSs is very low, the real part of complex permeability is thus close to 1.0 and the imaginary part is close to 0.0, which are far less than the parts of complex permittivity.[33,34] In addition, the complex permeability is defined as a constant because it is far less than complex permittivity. The convection heat transfer parameter is $k_0 = 10\ \mathrm{W/(m^2{\cdot}K)}$ and the surrounding temperature is $T_0 = 300$ K.

Based on the above mechanism of photothermal conversion (see detailed Supporting Information: Mechanism of photothermal conversion), the calculative and experimental results are presented in Figure 3b. The temperature of G/GNSs lenslet (at a concentration of 0.04 mg/mL) rose by 20 °C in 120 s, while the temperature of lenslets without GNSs undergoes significant changes upon nIR irradiation. So, without GNSs, lenslets possess negligible profile changes under nIR irradiation (Figure S3).

This remarkable photothermal conversion results in a transfer of energy from GNSs to environmental droplet in the form of thermal dissipation. In addition, for each lenslet, the Biot number $B_{iD} = (k_0 I/\lambda_{eff}) = (k_0 R/\lambda_{eff}) \approx 5.7 \times 10^{-7} \ll 1$ means that each lenslet has consistent internal temperature.[35] k_0 is convection heat transfer parameter, I is characteristic length of lenslet, and λ_{eff} is equivalent thermal conductivity of lenslet. Therefore, based on the theory of thermodynamics conduction,[35] temperature differences inside lenslet can be ignored.

The temperature increase resulting from photothermal conversion will cause a change in pressure difference P across the air–solution interface, with P directly determining the geometry of liquid meniscus. In Adamson's theoretical model,[36,37] the contact angle θ can be expressed in the following equation:

$$\cos\theta = 1 + C(T_c - T)^{a/(b-a)} \quad (5)$$

where T_c represents a critical temperature at which contact angle goes to zero, C is integration constant, and a and b are temperature-independent constants from a balance of intermolecular forces. Initially, owing to minimization of Gibbs free energy, the equilibrium contact angle θ_e is determined by a balance of solid–vapor γ_{SV}, solid–liquid γ_{SL}, and liquid–vapor surface γ tensions: $\cos\theta_e = (\gamma_{SV} - \gamma_{SL})/\gamma$, which is also known as Young's law.[38] However, when the droplet is actuated by nIR irradiation, the balance is off and the contact line of the lenslet moves along the template surface, which is different from that in equilibrium. As demonstrated in Figure 3c and d, before nIR irradiation, the lenslet remains static. When nIR irradiation is switched on, GNSs-activated photothermal conversion makes lenslets extravasate from microcavity. Once the nIR laser switches off, cold-contraction makes lenslets contract to the microcavity. These experimental results illustrate the reversibility of lenslet via switching nIR irradiation, meaning that the photothermal strategy can effectively regulate the lenslet meniscus by virtue of GNS-based photothermal conversion.

DOI: 10.1021/acsami.5b06361
ACS Appl. Mater. Interfaces 2015, 7, 21416–21422

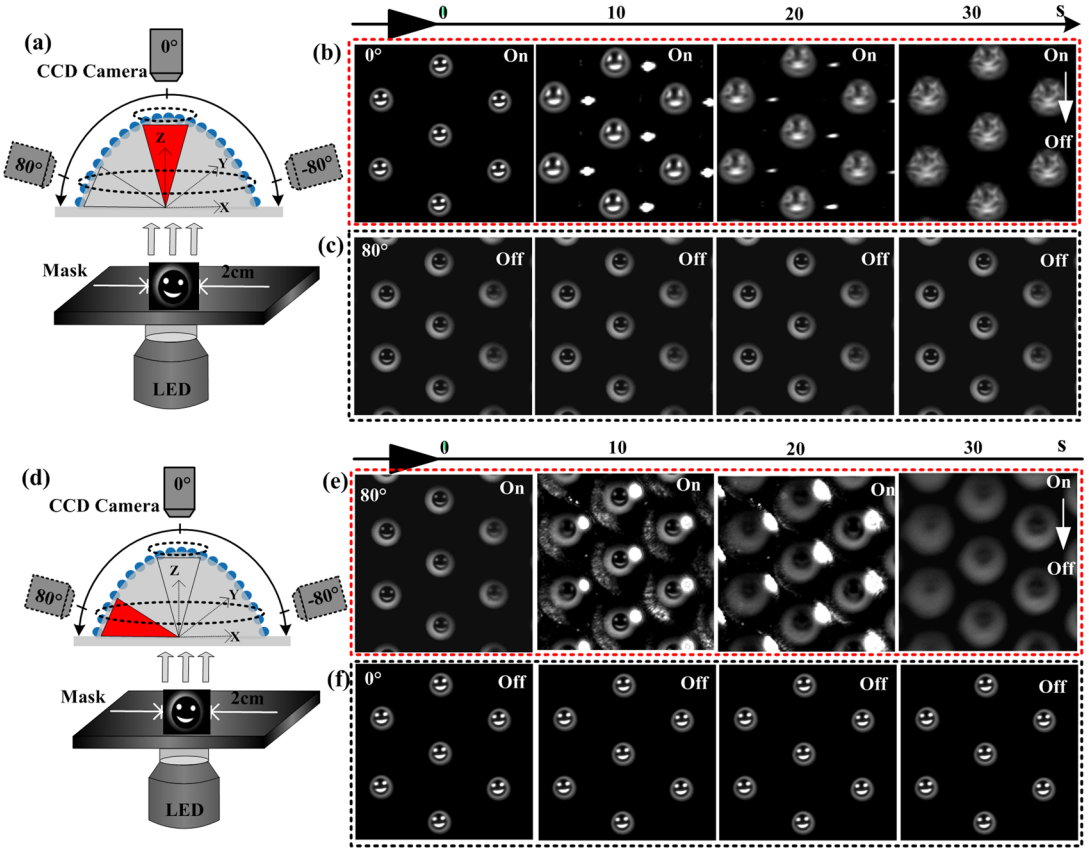

Figure 4. Programmable focusing capability of BCEs: sequentially irradiating BCEs at two angles of 0° (a) and 80° (d). The corresponding imaging information at 0° and 80° at different irradiation time (e.g., 0, 10, 20, and 30 s) are shown in (b) and (e), respectively. The local lenslets at (c) 80° and (f) 0° are always in focus.

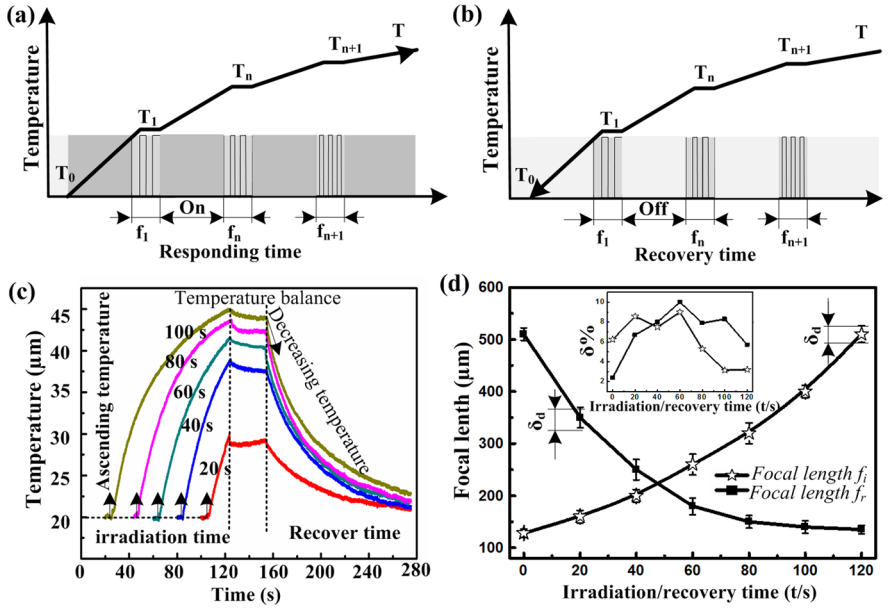

Figure 5. Under nIR laser pulses, irradiation time (a) and recovery time (b) dependence of lenslet temperature. (c) For each cycle process, the time-dependent temperature. (d) Focal length is plotted as a function of irradiation time and recovery time, respectively. The inset in (d) is the stability of BCEs by repeatable actuation after 1 week.

3.3. Programmable Focusing of BCEs. The key characteristic of the fabricated BCEs is the vari-focal capability, which benefits BCEs to dynamically track motion of tiny objects. Here, the vari-focal capability of nIR light-responsive BCEs was investigated by angular acceptance.[39] In order to avoid environmental disturbance, the nIR-actuated strategy was conducted in a superclean laboratory with constant temperature (20 °C) and humidity (50%). Two CCDs detected the related

DOI: 10.1021/acsami.5b06361
ACS Appl. Mater. Interfaces 2015, 7, 21416−21422

imaging information on BCEs at designated areas of 0° and 80° (Figure 4a and d). As irradiation time gradually varied from 0 to 30 s, the detected images of lenslets at 0° changed from clear to blurry (from in focus to defocused state) (Figure 4b and Video 1). Simultaneously, images in the area of 80° remained clear (Figure 4c). Similarly, when the nIR light was turned on at the area of 80° and off at 0° (Figure 4d), the local lenslets at 80° changed from in focus to defocused state (Figure 4e and Video 2). During this time, the local lenslets at 0° was always in focus (Figure 4f). Interestingly, given that the diffraction-limited diameter of the laser spot is 266 nm, it is theoretically possible to control a single G/GNSs lenslet. As a remote stimulus, nIR possesses the advantage of transmitting through tissue with relatively little attenuation and favorable biosafety to minimize the side effects on the adjacent region. Thus, in this work, nIR was utilized to drive the BCEs with programmable vari-focal ability.

Focal length is an important parameter to fulfill the vari-focal capability for microlenses. Based on the light-actuated strategy above, the increased radius of curvature R resulted in enhanced focal length. So, in order to realize a constant focal length, laser pulses with certain frequency (f_1, f_2,⋯, f_n) was adopted to maintain the expectant temperature (see Video 3). As demonstrated in Figure 5a and b, to keep a larger focal length, irradiation time and recovery time demanded a larger frequency ($f_{n+1} > f_n$) for a higher temperature. This behavior was ascribed to a faster energy loss $Q_{out} = \rho c_\nu (\partial T/\partial t)$ at a higher temperature. Herein, laser pulses were selectively modulated to reach a specific temperature (Figure 5c) for the desired focal length (Figure 5d). BCEs showed an ascending focal length f_i under nIR irradiation and reduced focal lengths f_r as switching light off. When temperature changed from 20 °C (at $t_i = 0$ s or $t_r = 120$ s) to 44 °C (at $t_i = 120$ s or $t_r = 0$ s), the focal lengths of f_i and f_r increased from 127 to 510 μm. Obviously, when temperature was less than 35 °C, focal length was passive to irradiation time and recovery time. As long as temperature was more than 44 °C, focal length became highly sensitive to irradiation time and recovery time. Similarly, BCEs were tunable by varying laser power (Figure S4and Video 4). Comprared to lower laser power of 1.0 W/cm^2, higher laser power led to larger imaging changes under the same irradiation time (Figure S4). Accordingly, this experiment was performed under a laser power of 2 W/cm^2. In addition, the reversibility is another key indicator to evaluate the performance of vari-focal lenses. Thus, the point spread function of graphene-based lenslets was also measured in our experiment. Along with increased recovery time, the light intensity gradually became larger and recovered to original state (Figure S5 and S6). This excellent reversibility of lenslet curvature indicates recurrent imaging activity of graphene-based BCEs.

The stability of BCEs was studied over 1 week by multicycle actuation. As illustrated in inset of Figure 5d, the focal length deviation δ_{de} among samples was less than 5 μm. A dimensionless parameter $\delta\% = \delta_{de}/\delta_{max}$ was defined to depict the repeatability of focal length curves during irradiation/recovery time, where δ_{max} denoted focal length induced by irradiation/recovery time. As illustrated in the inset of Figure 5d, δ% changed between 2% and 10%, indicating that the fabricated BCEs possessed outstanding stability under multicycle actuation.

For an application in 3-D microscopy of successive objects, a tunable-focus G/GNSs lens with a diameter of 800 μm was utilized. Frames in the scanning cycle (Figure S7 and Video 5) indicated that graphene-based lenses had a vari-focal ability from microscale to millimeter-scale.

4. CONCLUSION

In this work, based on photothermal conversion mechanisms, GNSs are utilized to fabricate novel and sensitive photo-responsive BCEs which feature large FOV, sensitive vari-focal capability, superior remote actuating, and programmable focusing. Meanwhile, BCEs have excellent imaging reversibility and repeatability. Considering that light actuation absolutely avoids mechanical and electronic disturbances, BCEs could be precisely operated under complicated work environments, providing promising applications in intelligent remote-driven systems.

■ ASSOCIATED CONTENT

Ⓢ Supporting Information

The Supporting Information is available free of charge on the ACS Publications website at DOI: 10.1021/acsami.5b06361.

Synthesis of GNSs, Microfabrication of BCEs, Mechanism of photothermal conversion, G/GNSs lens array actuated by various laser powers, Light intensity distribution of BCEs responding to nIR irradiation, and Sequence images of two objects from G/GNSs lens (PDF)
Imaging of BCEs with GNSs at the area of 0°= (AVI)
Imaging of BCEs with GNSs at the area of 80° (AVI)
BCEs with GNSs maintaining an expectant temperature (AVI)
BCEs with GNSs actuated by varying laser power (AVI)
Imaging of two successive objects (AVI)

■ AUTHOR INFORMATION

Corresponding Authors

*E-mail: hzliu@mail.xjtu.edu.cn.
*E-mail: wtjiang@mail.xjtu.edu.cn.

Author Contributions

#Lanlan Wang and Fang Li contributed equally to this work. They are both the first author.

Notes

The authors declare no competing financial interest.

■ ACKNOWLEDGMENTS

This work is supported by National Natural Science Foundation of China (Grants 91323303, 51275400 and 51405372). This work is partially sponsored by the Specialized Research Fund for the Doctoral Program of Higher Education (Grants 20130201120036 and 2014T70912).

■ REFERENCES

(1) Wu, M.-H.; Whitesides, G. M. Fabrication of Diffractive and Micro-optical Elements Using Microlens Projection Lithography. *Adv. Mater.* **2002**, *14*, 1502−1506.

(2) Song, Y. M.; Xie, Y.; Malyarchuk, V.; Xiao, J.; Jung, I.; Choi, K. J.; Liu, Z.; Park, H.; Lu, C.; Kim, R. H.; et al. Digital Cameras with Designs Inspired by the Arthropod Eye. *Nature* **2013**, *497* (7447), 95−99.

(3) Tsutsumi, N.; Kinashi, K.; Tada, K.; Fukuzawa, K.; Kawabe, Y. Fully Updatable Three-Dimensional Holographic Stereogram Display Device Based on Organic Monolithic Compound. *Opt. Express* **2013**, *21* (17), 19880−19884.

(4) Li, Z.; Xiao, J. Mechanics and Optics of Stretchable Elastomeric Microlens Array for Artificial Compound Eye Camera. *J. Appl. Phys.* **2015**, *117* (1).01490410.1063/1.4905299

(5) Jeong, K.-H.; Kim, J.; Lee, L. P. Biologically Inspired Artificial Compound Eyes. *Science* **2006**, *312* (5773), 557−561.

(6) Liu, H.; Chen, F.; Yang, Q.; Qu, P.; He, S.; Wang, X.; Si, J.; Hou, X. Fabrication of Bioinspired Omnidirectional and Gapless Microlens

Array for Wide Field-of-view Detections. *Appl. Phys. Lett.* **2012**, *100* (13), 133701.
(7) Snyder, A. W.; Stavenga, D. G.; Laughlin, S. B. Spatial Information Capacity of Compound Eyes. *J. Comp. Physiol.* **1977**, *116* (2), 183−207.
(8) Floreano, D.; Pericet-Camara, R.; Viollet, S.; Ruffier, F.; Bruckner, A.; Leitel, R.; Buss, W.; Menouni, M.; Expert, F.; Juston, R.; Dobrzynski, M. K.; L'Eplattenier, G.; Recktenwald, F.; Mallot, H. A.; Franceschini, N. Miniature Curved Artificial Compound Eyes. *Proc. Natl. Acad. Sci. U. S. A.* **2013**, *110* (23), 9267−9272.
(9) Dong, L.; Agarwal, A. K.; Beebe, D. J.; Jiang, H. Adaptive Liquid Microlenses Activated by Stimuli-responsive Hydrogels. *Nature* **2006**, *442* (7102), 551−554.
(10) Artal, P.; Benito, A.; Tabernero, J. The Human Eye is an Example of Robust Optical Design. *Journal of Vision* **2006**, *6* (1), 1−7.
(11) Wu, D.; Wang, J. N.; Niu, L. G.; Zhang, X. L.; Wu, S. Z.; Chen, Q. D.; Lee, L. P.; Sun, H. B. Bioinspired Fabrication of High-Quality 3D Artificial Compound Eyes by Voxel-Modulation Femtosecond Laser Writing for Distortion-Free Wide-Field-of-View Imaging. *Adv. Opt. Mater.* **2014**, *2* (8), 751−758.
(12) Huang, C. C.; Wu, X.; Liu, H.; Aldalali, B.; Rogers, J. A.; Jiang, H. Optics: Large-Field-of-View Wide-Spectrum Artificial Reflecting Superposition Compound Eyes. *Small* **2014**, *10* (15), 3050−3057.
(13) Miccio, L.; Paturzo, M.; Grilli, S.; Vespini, V.; Ferraro, P. Hemicylindrical and Toroidal Liquid Microlens Formed by Pyroelectro-wetting. *Opt. Lett.* **2009**, *34* (7), 1075−1077.
(14) Ren, H.; Wu, S.-T. Tunable-focus Liquid Microlens Array Using Dielectrophoretic Effect. *Opt. Express* **2008**, *16* (4), 2646−2652.
(15) Zhang, W.; Aljasem, K.; Zappe, H.; Seifert, A. Completely Integrated, Thermo-Pneumatically Tunable Microlens. *Opt. Express* **2011**, *19* (3), 2347−2362.
(16) Huang, N. T.; Zhang, H. L.; Chung, M. T.; Seo, J. H.; Kurabayashi, K. Recent Advancements in Optofluidics-based Single-cell Analysis: Optical on-chip Cellular Manipulation, Treatment, and Property Detection. *Lab Chip* **2014**, *14* (7), 1230−1245.
(17) Baffou, G.; Quidant, R. Thermo-plasmonics: Using Metallic Nanostructures as Nano-sources of Heat. *Laser & Photonics Reviews* **2013**, *7* (2), 171−187.
(18) Liang, C.; Diao, S.; Wang, C.; Gong, H.; Liu, T.; Hong, G.; Shi, X.; Dai, H.; Liu, Z. Tumor Metastasis Inhibition by Imaging-guided Photothermal Therapy with Single-walled Carbon Nanotubes. *Adv. Mater.* **2014**, *26* (32), 5646−5652.
(19) Li, M.; Yang, X.; Ren, J.; Qu, K.; Qu, X. Using Graphene Oxide High Near-Infrared Absorbance for Photothermal Treatment of Alzheimer's disease. *Adv. Mater.* **2012**, *24* (13), 1722−1728.
(20) Low, T.; Engel, M.; Steiner, M.; Avouris, P. Origin of Photoresponse in Black Phosphorus Phototransistors. *Phys. Rev. B: Condens. Matter Mater. Phys.* **2014**, *90* (8), 081408.10.1103/PhysRevB.90.081408
(21) Liu, G. L.; Kim, J.; Lu, Y.; Lee, L. P. Optofluidic Control Using Photothermal Nanoparticles. *Nat. Mater.* **2006**, *5* (1), 27−32.
(22) Liu, C.; Christopher, L. Three Dimensional Moving Pictures with a Single Imager and Microfluidic Lens. *IEEE Transactions on Consumer Electronics* **2014**, *60* (2), 258−266.
(23) Pierce, M. C.; Weigum, S. E.; Jaslove, J. M.; Richards-Kortum, R.; Tkaczyk, T. S. Optical Systems for Point-of-care Diagnostic Instrumentation: Analysis of Imaging Performance and Cost. *Ann. Biomed. Eng.* **2014**, *42* (1), 231−240.
(24) Borst, A.; Plett, J. Optical Devices: Seeing the World through an Insect's eyes. *Nature* **2013**, *497*, 47−48.
(25) Hummers, W. S.; Offeman, R. E. Preparation of Graphitic Oxide. *J. Am. Chem. Soc.* **1958**, *80* (6), 1339.
(26) Huh, C.; Scriven, L. E. Hydrodynamic Model of Steady Movement of a Solid/liquid/fluid Contact Line. *J. Colloid Interface Sci.* **1971**, *35* (71), 85−101.
(27) Dussan, E. B. On the Spreading of Liquids on Solid Surfaces: Static and Dynamic Contact Lines. *Annu. Rev. Fluid Mech.* **1979**, *11* (1), 371−400.
(28) Govorov, A. O.; Richardson, H. H. Generating Heat with Metal Nanoparticles. *Nano Today* **2007**, *2* (7), 30−38.
(29) Hornyak, G. L.; Patrissi, C. J.; Martin, C. R. Fabrication, Characterization, and Optical Properties of Gold Nanoparticle/Porous Alumina Composites: the Nonscattering Maxwell Garnett Limit. *J. Phys. Chem. B* **1997**, *101* (9), 1548−1555.
(30) Sugano, Y.; Takahashi, S. Material Design of Functionally Graded Plates with the Function of Electromagnetic Noise Suppression. *J. Solid Mech. Mater. Eng.* **2008**, *2* (7), 912−923.
(31) Tian, H. Y.; Wang, X. Z.; Zhou, Y. H. Thermoelastic Stress in a Functionally Graded in Finite Plate with Electromagnetic Wave Absorption. *Chin. Phys. Lett.* **2012**, *29* (11), 116801−1−4.
(32) Akerlof, G. Dielectric Constants of Some Organic Solvent-water Mixtures at Warious Temperatures. *J. Am. Chem. Soc.* **1932**, *54* (11), 4125−4139.
(33) Zhang, D. D.; Zhao, D. L.; Zhang, J. M.; Bai, L. Z. Microwave Absorbing Property and Complex Permittivity and Permeability of Graphene-CdS Nanocomposite. *J. Alloys Compd.* **2014**, *589*, 378−383.
(34) Zheng, J.; Lv, H.; Lin, X.; Ji, G.; Li, X.; Du, Y. Enhanced Microwave Electromagnetic Properties of Fe_3O_4/graphene Nanosheet Composites. *J. Alloys Compd.* **2014**, *589*, 174−181.
(35) Lee, S.; Salamon, N. J.; Sullivan, R. M. Finite Element Analysis of Poroelastic Composites Undergoing Thermal and Gas Diffusion. *J. Thermophys. Heat Transfer* **1996**, *10* (4), 672−680.
(36) Adamson, A. W. An Adsorption Model for Contact Angle and Spreading. *J. Colloid Interface Sci.* **1968**, *27* (2), 180−187.
(37) Adamson, A. W. Potential Distortion Model for Contact Angle and Spreading. II. Temperature Dependent Effects. *J. Colloid Interface Sci.* **1973**, *44*, 273−281.
(38) Verplanck, N.; Coffinier, Y.; Thomy, V.; Boukherroub, R. Wettability Switching Techniques on Superhydrophobic Surfaces. *Nanoscale Res. Lett.* **2007**, *2* (12), 577−596.
(39) Yong, J.; Chen, F.; Yang, Q.; Du, G.; Bian, H.; Zhang, D.; Si, J.; Yun, F.; Hou, X. Rapid Fabrication of Large-area Concave Microlens Arrays on PDMS by a Femtosecond Laser. *ACS Appl. Mater. Interfaces* **2013**, *5* (19), 9382−9385.

DOI: 10.1021/acsami.5b06361
ACS Appl. Mater. Interfaces 2015, 7, 21416−21422